Science Advances
AAAS

advances.sciencemag.org/cgi/content/full/5/7/eaaw3808/DC1

Supplementary Materials for

Structural basis for the multitasking nature of the potato virus Y coat protein

Andreja Kežar, Luka Kavčič, Martin Polák, Jiří Nováček, Ion Gutiérrez-Aguirre, Magda Tušek Žnidarič, Anna Coll, Katja Stare, Kristina Gruden, Maja Ravnikar, David Pahovnik, Ema Žagar, Franci Merzel, Gregor Anderluh, Marjetka Podobnik*

*Corresponding author. Email: marjetka.podobnik@ki.si

Published 17 July 2019, *Sci. Adv.* **5**, eaaw3808 (2019)
DOI: 10.1126/sciadv.aaw3808

The PDF file includes:

Other Supplementary Material for this manuscript includes the following:

(available at advances.sciencemag.org/cgi/content/full/5/7/eaaw3808/DC1)

Data S1 (Microsoft Excel format). Relative concentration of PVY RNA as measured in the leaves of *N. clevelandii* including tables S3 to S5:

Table S3. Relative concentration of PVY RNA as measured in bombarded leaves of *N. clevelandii* 7 dpb (experiment 1).
Table S4. Relative concentration of PVY RNA as measured in upper nonbombarded leaves of *N. clevelandii* 14 dpb (experiment 1).
Table S5. Relative concentration of PVY RNA as measured in bombarded leaves of *N. clevelandii* (experiment 2).

Supplementary Text S1. Detailed description of protein-protein interactions in PVY

Numerous protein-protein interactions in the cluster of 13 interconnected CP units are translationally repeated along the axis of the viral filament (Fig. 2A and fig. S5). The CP^{n} N-terminal region stretches all the way to CP^{n-10} unit. The groove between the β-hairpin loop and helices α3 and α2 in CP^{n-10} core nests CP^{n} residues Val44 – Lys48 in a combination of electrostatic and hydrophobic interactions, and the same is true for the CP^{n+10} – CP^{n} interface (fig. S5A). Interactions between CP^{n} – CP^{n-2} (counterpart CP^{n+2} – CP^{n}) are limited to the salt bridge between Lys58 at the sharp turn in the N-terminal region of CP^{n}, and Asp138 in the loop of CP^{n-2} β-hairpin (fig. S5B). CP^{n} – CP^{n-1} interactions (counterpart CP^{n+1} – CP^{n}) are mainly based on CP^{n} residues Ala49 – Asn82 folding on the outer surface of the CP^{n-1} core (fig. S5C), with alternating electrostatic and hydrophobic interactions anchoring the N-terminal peptide of CP^{n} to the core of CP^{n-1}. The CP^{n} core sits on top of the CP^{n-8} and CP^{n-9} cores (fig. S5D). These interactions are mainly electrostatic and are mirrored by interactions between CP^{n}, CP^{n+8} and CP^{n+9} units. The C-terminal region of CP^{n} unit is completely defined and extends inside the lumen all the way up to the core of CP^{n+17} (Fig. 2A). The CP^{n} α8-helix (Val211 – Leu225) and the first residues of the extended C-terminal region, Lys226 – Arg231, are stacked between C-terminal regions of CP^{n-8} and CP^{n-9}, based on mixed electrostatic and hydrophobic interactions (fig. S5E). The following CP^{n} residues, Leu232 – Ile239, are sandwiched between α8-helices of CP^{n+8} and CP^{n+9}, the core residues Val187 – Arg191 of CP^{n+8}, and Asn245 – Thr251 of CP^{n-9} (fig. S5F). CP^{n} residues Ser240 – Thr251 run along Ser227 – Ile239 of CP^{n+9}, while Ser227 – Ile239 in the neighboring CP^{n+8} deviate away from CP^{n} to run along Thr240 – Thr251 of CP^{n-1} (fig. S5G). C-terminal residues Glu244 – Glu252 of CP^{n} run in parallel along the α8-helix of CP^{n+17}, predominantly based on electrostatic interactions (fig. S5H). Due to helical symmetry, the α8-helix of CP^{n} interacts in the same manner with C-terminal residues of CP^{n-17}. The interactions of approximately 20 final residues (Glu247 – Met267) further strengthen the contacts between CP^{n} and CP^{n-1} (fig. S5I). After Thr251, the extended C-terminal peptide of CP^{n} undergoes two sharp turns, which end in Thr260, from which it extends to the final residue Met267 again, but this time in almost perpendicular direction to the filament. This final region (Thr260 – Met267) is sandwiched between similar regions of CP^{n-1} and CP^{n+1} (fig. S5I).

Supplementary Text S2. Detailed description of protein-protein interactions in VLP

The interaction network in VLPs is decreased to only five CPs (Fig. 3D), not taking into account potential random interactions between the flexible C-terminal regions. Each ring is held together via interactions between neighboring core domains. Similar to authentic virions, the N-terminal region between residues Met54 and Ala85 of CP^{n} acts as a clip and fixes CP^{n} onto the core of CP^{n-1} (Figs. 3, C to E). Electrostatic interactions prevail (fig. S8), with a patch of hydrophobic interactions between α1-helix of CP^{n} and α5 of CP^{n-1} core (Fig. 3E, fig. S8B). The inter-ring connection is limited to interactions between the extended region of residues Thr43 to Ala49 of CP^{n} and those of the α-hairpin loop and helices α2 - α4 of CP^{i-2} (Fig. 3E). In contrast to virions (Fig. 1D), there is no interaction between the N-terminal region of CP^{n} and CP^{n-2} in VLP.

Supplementary Text S3. Importance of the CP N terminus for longitudinal assembly of VLPs

To study the importance of the N-terminal region in longitudinal assembly of octameric VLP rings, N-terminal deletion mutants were prepared (Fig. 5, A and B). Of these, only the mutant proteins ΔN49 and ΔN69 were soluble (Fig. 5B) and both had circular dichroism spectra comparable to wild-type CP (fig. S3E). SEC-MALS analysis of purified ΔN49 protein revealed a 210 kDa complex, consistent with the octameric assembly of ΔN49 (fig. S3D). In addition, a smaller population of high molecular weight aggregates were also present, which were not filamentous structures, as confirmed by negative stain TEM (Fig. 5B, middle panel). Based on the VLP interaction network, ΔN49 should form octameric rings and ΔN69 should remain monomeric (Fig. 3E). Indeed, cryo-EM revealed that ΔN49 oligomers were octameric rings with the tendency to adhere to each other, thereby forming stacks of up to four rings (Fig. 5B, bottom panel). No filaments were detected for ΔN69 (Fig. 5B, middle panel) and SEC-MALS detected monomers and unspecific aggregates (fig. S3D).

Supplementary Text S4. Redundancy of CP C termini for VLP filament or octameric ring

CP C-terminal deletion mutant proteins were prepared to assay the impact of the disordered C-terminus on VLP filament shape and stability (Fig. 5, A and C). These mutant proteins were all soluble, and similarly to PVY virions and VLPs formed from wild-type CP, partial proteolysis could be observed in final purified samples (Fig. 5C, upper panel right, fig. S3C). Interestingly, filament formation was preserved even in the absence of the 60 C-terminal residues, e.g. up to Ser207, which is located at the start of the final α8-helix (Fig. 5C, middle and bottom panels). We further purified and characterized ΔC40, which still includes the α8 helix, and ΔC60, which lacks it. Circular dichroism spectra (fig. S3E) and negative stain TEM images of purified VLPs formed of ΔC40 and ΔC60 (Fig. 5C, middle and bottom panel right) were comparable to wild-type VLPs (fig. S7A). In the case of ΔC40 VLPs we could observe the inner channel of the filament (Fig. 5C, middle panel right, inset).

We prepared a double deletion mutant, ΔN49C40 (Fig. 5, A and D), to remove the flexible C-terminal extension still present in the octameric ring of ΔN49. Interestingly, in addition to octameric rings detected by SEC-MALS (fig. S3D), loosely bound filaments (generally less than 500 nm long) were detected by negative stain TEM (Fig. 5D, upper and middle panel left), which were significantly longer than ΔN49-derived stacks of rings (Fig. 5B bottom). This showed that the C-terminal region is not only dispensable for VLP filament formation, but may even contribute to its destabilization. Indeed, after we removed the C-termini of deletion mutants ΔN29 and ΔN39 (which were insoluble), the resulting ΔN29C40 and ΔN39C60 proteins could form long filaments (Fig. 5D).

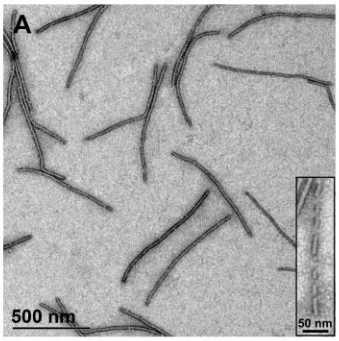
A
500 nm
50 nm

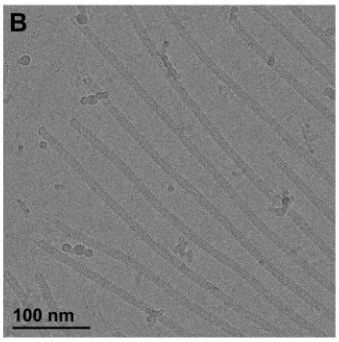
B
100 nm

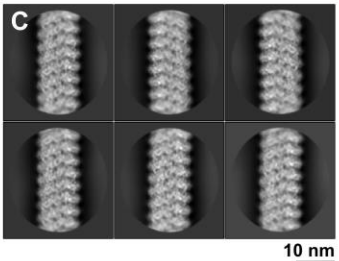
C
10 nm

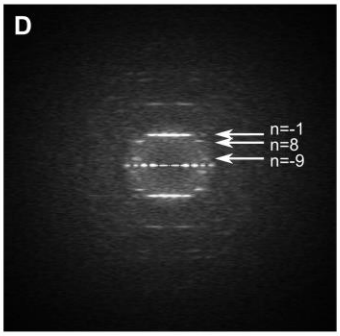
D
n=-1
n=8
n=-9

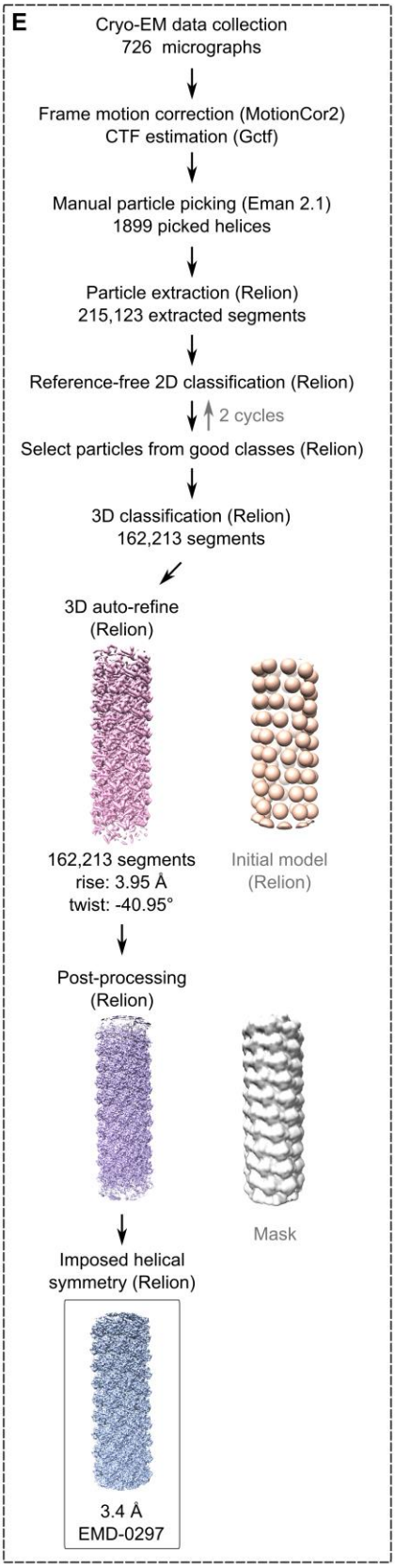
E
Cryo-EM data collection
726 micrographs
Frame motion correction (MotionCor2)
CTF estimation (Gctf)
Manual particle picking (Eman 2.1)
1899 picked helices
Particle extraction (Relion)
215,123 extracted segments
Reference-free 2D classification (Relion)
2 cycles
Select particles from good classes (Relion)
3D classification (Relion)
162,213 segments
3D auto-refine
(Relion)
162,213 segments
rise: 3.95 Å
twist: -40.95°
Initial model
(Relion)
Post-processing
(Relion)
Mask
Imposed helical
symmetry (Relion)
3.4 Å
EMD-0297

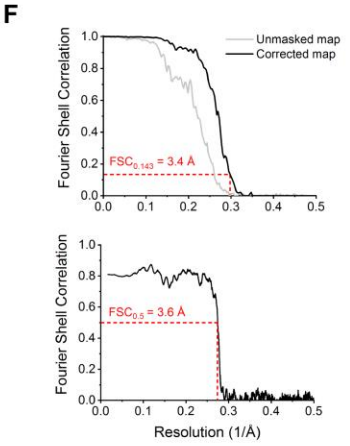
F
Unmasked map
Corrected map
Fourier Shell Correlation
FSC0.143 = 3.4 Å
FSC0.5 = 3.6 Å
Resolution (1/Å)

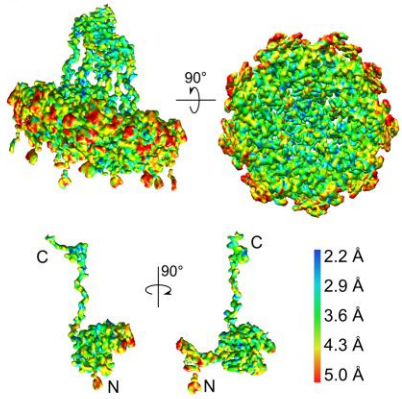
G
90°
C
N
2.2 Å
2.9 Å
3.6 Å
4.3 Å
5.0 Å

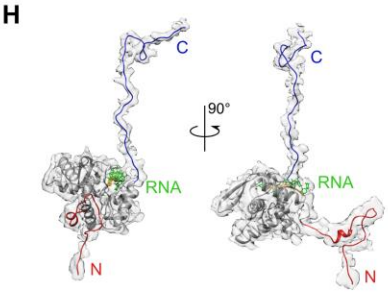
H
C
90°
RNA
N

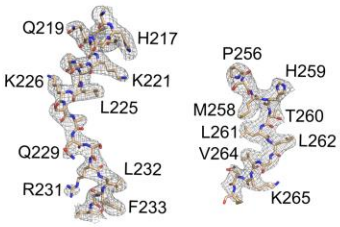
I
Q219
H217
K226
K221
L225
Q229
L232
R231
F233
P256
H259
M258
T260
L261
L262
V264
K265

Fig. S1. Cryo-EM data collection, image processing, and model building for the PVY virion. (**A**) Negative-stain TEM micrograph of PVY. Inset: an example of a damaged PVY filament. (**B**) Cryo-EM micrograph of PVY. (**C**) Examples of PVY 2D class averages. (**D**) Sum of the power spectra obtained for 53 selected PVY segments. The black lines highlight the n = -1 layer line at 1/35 Å, the n = 8 layer line at 1/43 Å, and n = -9 layer line at 1/160 Å corresponding to one-start left-handed helix. (**E**) Flowchart of the data collection and processing for the PVY virion. (**F**) Fourier shell correlation (FSC) curves for the final reconstruction of PVY density map (top) and between the PVY model and density map (bottom). (**G**) Local resolution analysis of one turn of the PVY filament (top) and one extracted CP unit (below), estimated using MonoRes (*34*). (**H**) Surface representation of density map with a structural model of PVY CP (N-terminal region: red, core: gray, C-terminal region: blue). (**I**) The densities of two PVY CP segments are shown in a mesh representation (maps contoured at 3σ) with the corresponding atomic model within, showing the resolution of individual side chains.

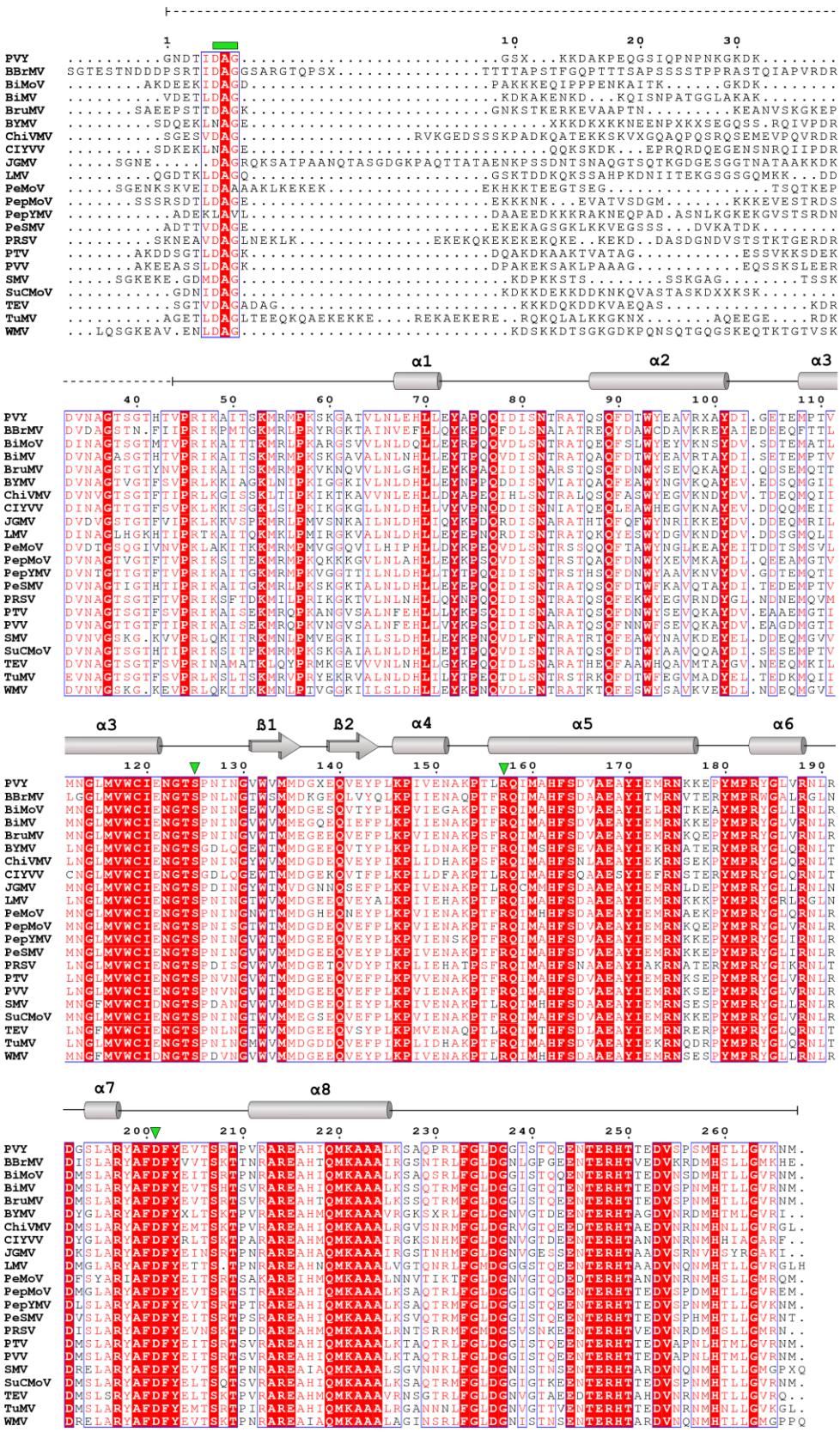
α1
α2
α3
ß1
ß2
α4
α5
α6
α7
α8
PVY
BBrMV
BiMoV
BiMV
BruMV
BYMV
ChiVMV
CIYVV
JGMV
LMV
PeMoV
PepMoV
PepYMV
PeSMV
PRSV
PTV
PVV
SMV
SuCMoV
TEV
TuMV
WMV

Fig. S2. Consensus sequence alignment of potyviral CPs. CP sequences of PVY (36), banana bract mosaic virus (BBrMV) (64), Bidens mottle virus (BiMoV) (9), Bidens mosaic virus (BiMV) (4), Brugmansia mosaic virus (BruMV) (5), bean yellow mosaic virus (BYMV) (45), chilli veinal mottle virus (ChiVMV) (15), clover yellow vein virus (ClYVV) (13), johnsongrass mosaic virus (JGMV) (28), lettuce mosaic virus (LMV) (12), peanut mottle virus (PeMoV) (12), pepper mottle virus (PepMoV) (7), pepper yellow mosaic virus (PepYMV) (10), pepper severe mosaic virus (PeSMV) (5), papaya ringspot virus (PRSV) (44), Peru tomato mosaic virus (PTV) (6), potato virus V (PVV) (32), soybean mosaic virus (SMV) (59), sunflower chlorotic mottle virus (SuCMoV) (5), tobacco etch virus (TEV) (77), turnip mosaic virus (TuMV) (73) and watermelon mosaic virus (WMV) (54) were obtained from NCBI database (https://www.ncbi.nlm.nih.gov/) (number of sequences for each CP is in brackets) and aligned with ClustalW algorithm in MEGA7 (*56*). Consensus sequences were created in BioEdit (*57*) and aligned using identity protein weight matrix in MEGA7. 'X': non-consensus positions at frequency threshold of 60 %. The alignment is presented using ESPript 3.0 (http://espript.ibcp.fr/ESPript/ESPript/). Green box: the conserved DAG site; green arrows: conserved RNA binding residues. Above: a scheme of PVY CP secondary structure.

A

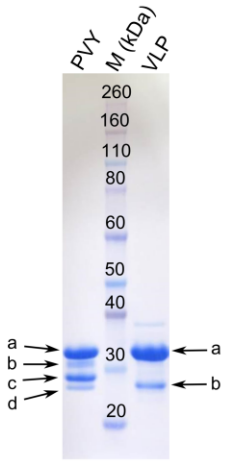

B

	SDS-PAGE band	N-terminal sequence	Deletion*
PVY	a	GNDTI	/
		DAGGS	ΔN5
		NVGTS	ΔN34
	b	GNDTI	/
		KDAKQ	ΔN12
		KQEQG	ΔN15
	c	DAGGS	ΔN5
		QEQGS	ΔN16
		KEKEK	ΔN27
	d	APQQI	ΔN73
		TSPNI	ΔN123
VLP	a	GNDTI	/
	b	NA**	NA**

* Number of deleted amino acids from N-terminus, based on the reads from Edman sequencing. ** The N-terminal sequence was not readable.

C

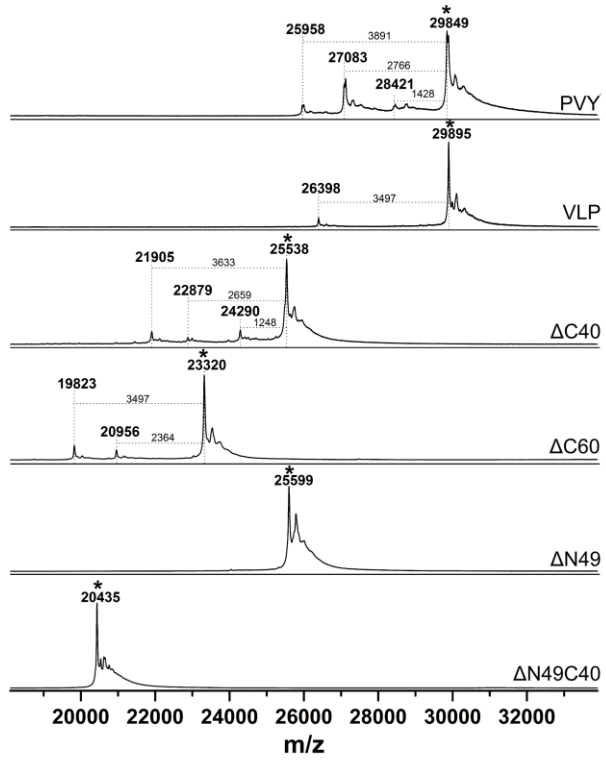

D

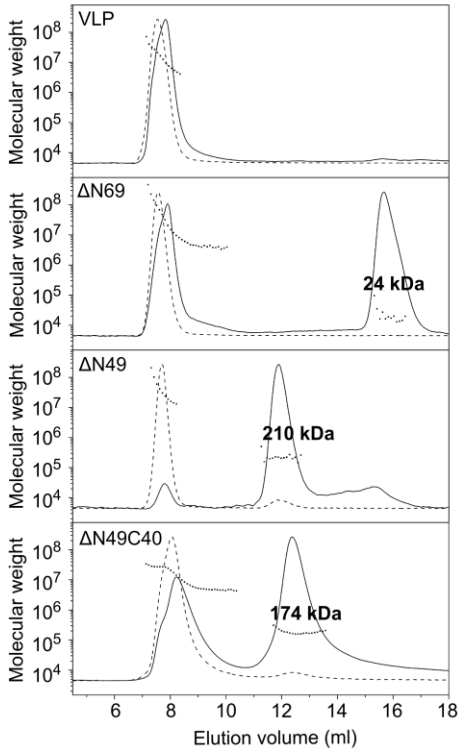

E

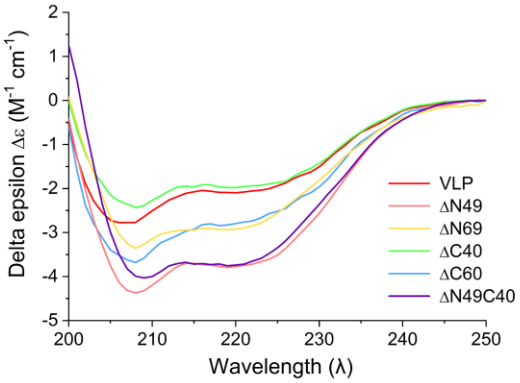

Fig. S3. Biophysical characterization of PVY virions and various VLP constructs. (**A**) SDS-PAGE bands transferred to a PVDF membrane reveal proteolysis of the CP in both the PVY and VLP samples. (**B**) Edman sequencing of bands in (A). The intact CP unit is found in band 'a' of both, PVY and VLP, while additional lower bands 'b-d' represent proteolysed CP units. Sequence reads of each band are displayed together with their assigned number of missing N-terminal amino acids. (**C**) Comparison of MALDI-TOF mass spectra of PVY and different VLP constructs. The peaks corresponding to full-length proteins are marked with *. Peaks at smaller m/z representing truncated protein species are observed in all the spectra except for ΔN49 and ΔN49C40. (**D**) SEC-MALS chromatograms (solid lines: UV response, dashed lines: light scattering response at 90° angle) for wild-type VLP filaments and non-filamentous constructs ΔN69, ΔN49 and ΔN49C40. (**E**) Circular dichroism spectra of wild-type VLP and deletion mutants ΔN49, ΔN69, ΔC40, ΔC60 and ΔN49C40.

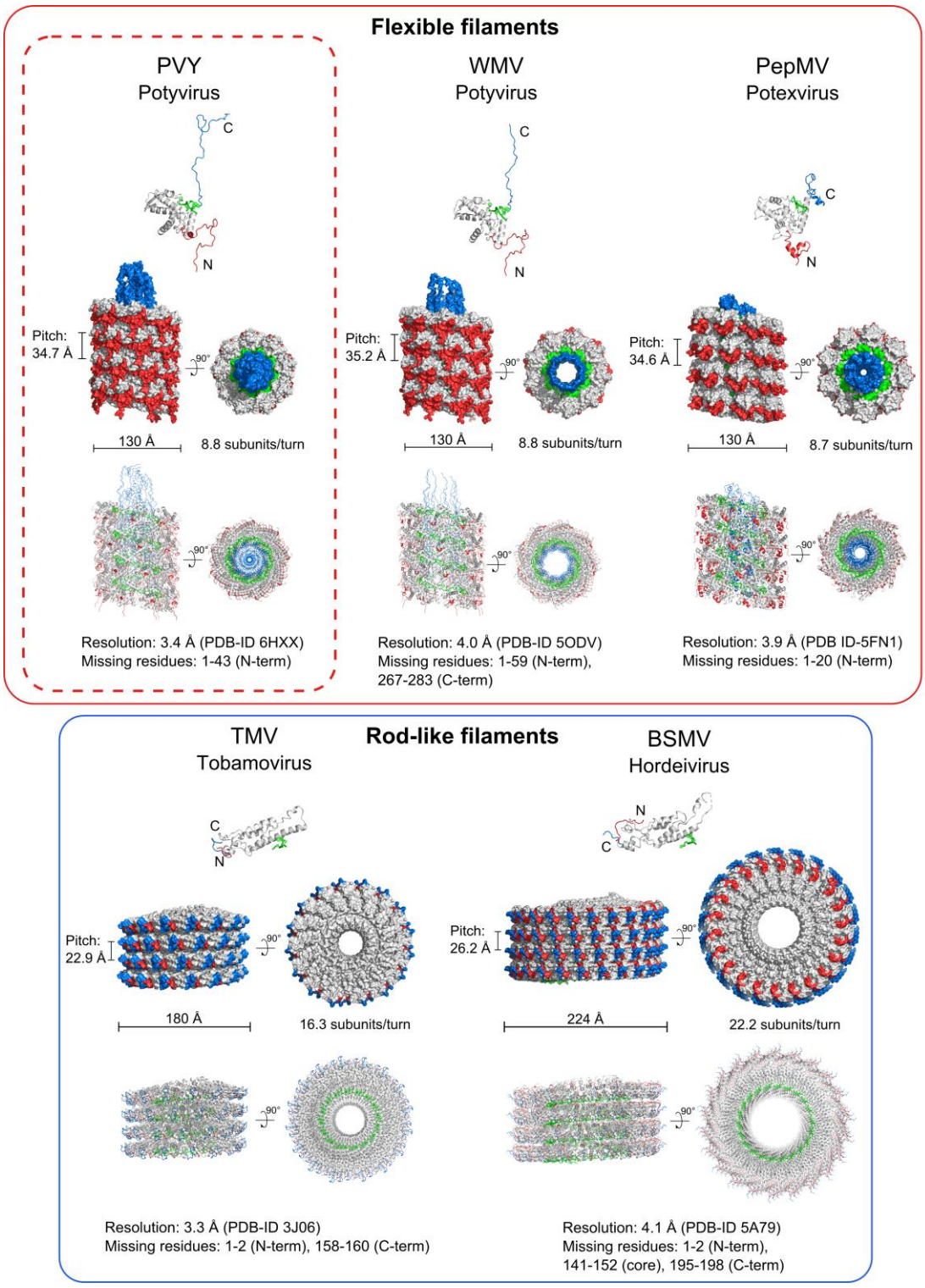

Fig. S4. Structural comparison of PVY to other filamentous viruses, flexible and rod shaped. For all viruses, the structure of a single CP unit is shown in cartoon, N-terminal region in red, core in gray, C-terminal region in blue and RNA in green color. Viral filaments are shown in surface and cartoon representation, side and top-view.

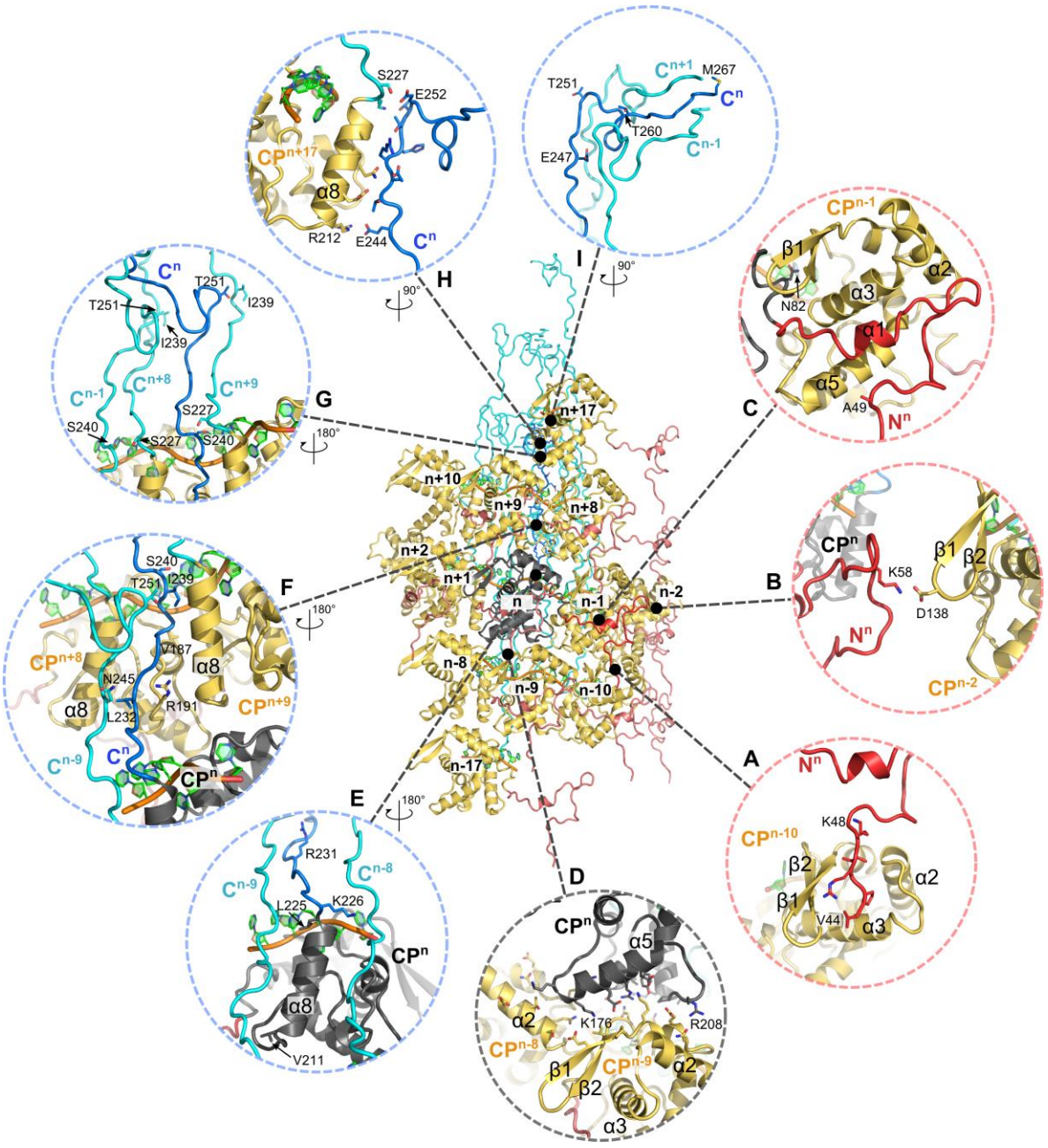

Fig. S5. Details of the PVY interaction network. Assembly of 13 interacting CP units is presented in the center of the figure. CP^{n} N-terminal region is in red, core in dark gray and C-terminal region in blue, while neighboring CPs are colored in light red (N-terminal region), yellow (core) and light blue (C-terminal region). Close-up views display specific interaction sites between CP units (red circles display interactions given by the CP^{n} N-terminal region, black circle the interactions between the cores, and blue circles show interactions given by CP^{n} C-terminal region). For clarity, some non-interacting parts were removed from the picture. The interactions between CP units are presented from CP^{n} N- to C-terminus: (**A**) CP^{n} – CP^{n-10}, (**B**) CP^{n} – CP^{n-2}, (**C**) CP^{n} – CP^{n-1}, (**D**) CP^{n} – CP^{n-8} – CP^{n-9}, (**E**) CP^{n} – CP^{n-8} – CP^{n-9}, (**F**) CP^{n} – CP^{n-9} – CP^{n+8} – CP^{n+9}, (**G**) CP^{n} – CP^{n+8} – CP^{n+9} – CP^{n-1}, (**H**) CP^{n} – CP^{n+17} and (**I**) CP^{n} – CP^{n+1} – CP^{n+1}.

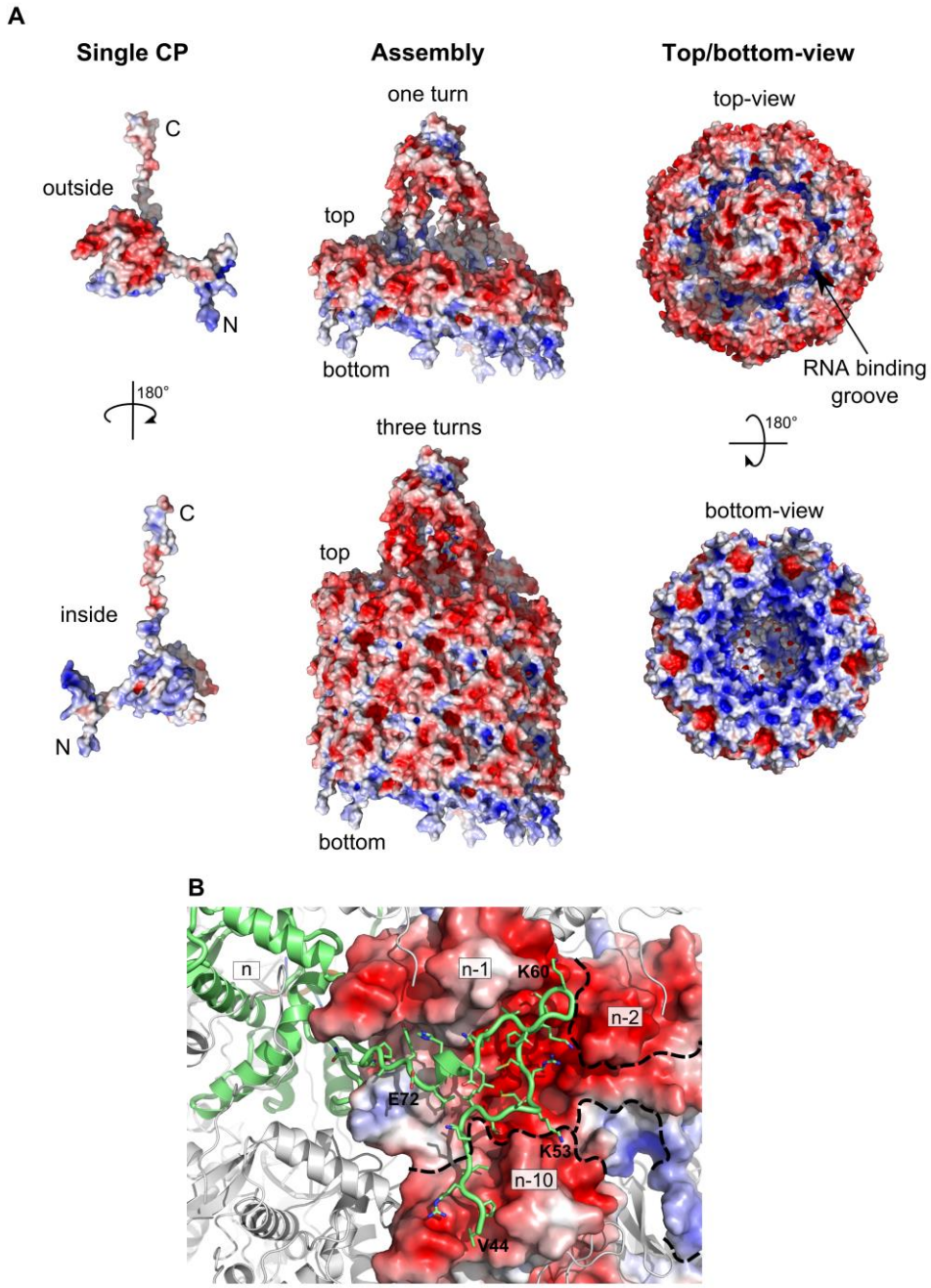

Fig. S6. Electrostatic interactions are crucial for PVY virion assembly. (**A**) Surface electrostatic potential (red: negative charge; blue: positive charge) of a single CP unit (left); CP units assembled into one turn (above center) and the filament (below center). Right: top- and bottom-view of the filament. The RNA-binding groove is highly positively charged to bind viral ssRNA. (**B**) Highly negatively charged surface of neighboring units CP^{n-1}, CP^{n-2} and CP^{n-10} promote folding of positively charged CP^{n} N-terminal region on their surface. The CP^{n} unit is shown as a green cartoon.

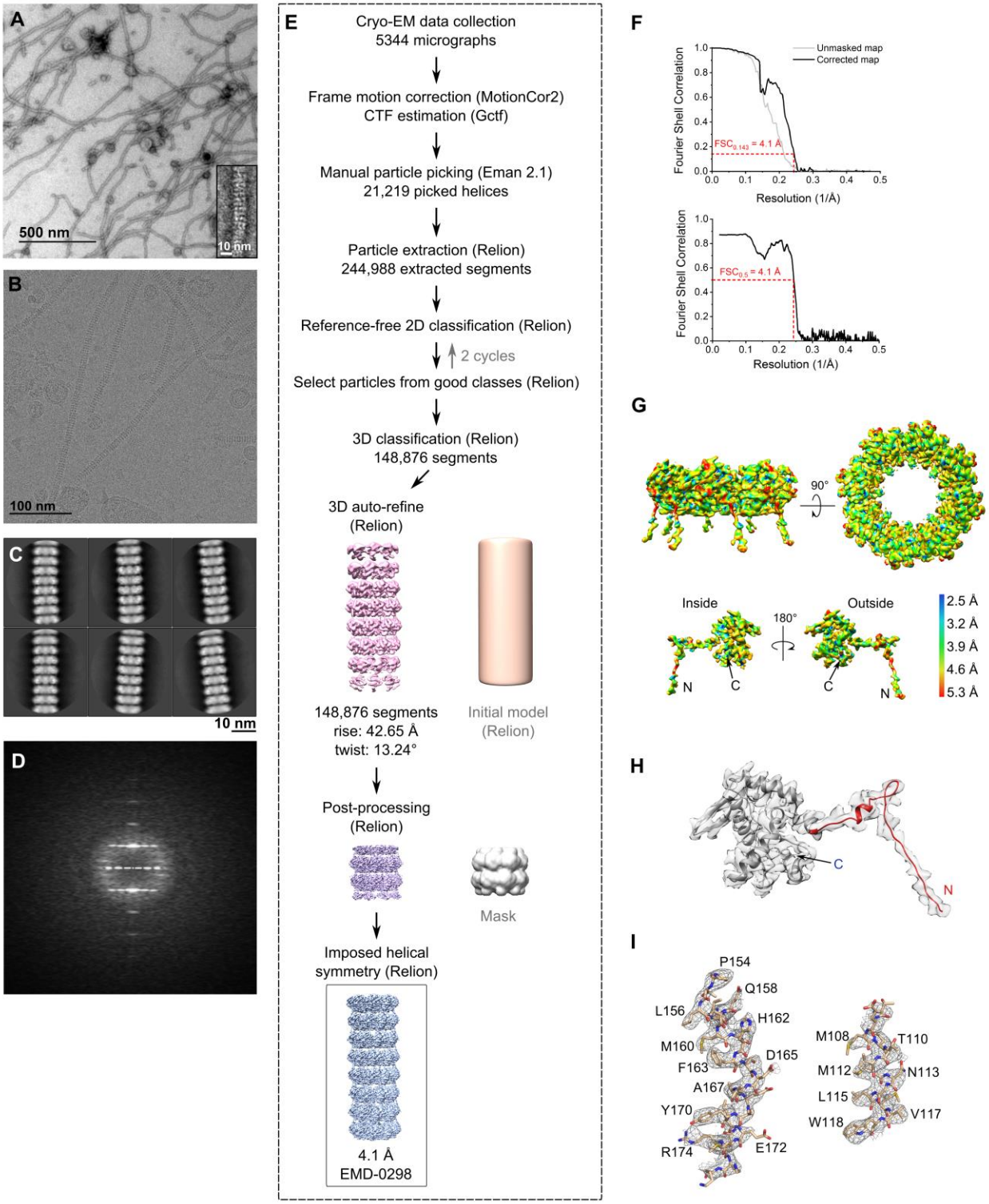
A
500 nm
10 nm
B
100 nm
C
10 nm
D
E
Cryo-EM data collection
5344 micrographs
Frame motion correction (MotionCor2)
CTF estimation (Gctf)
Manual particle picking (Eman 2.1)
21,219 picked helices
Particle extraction (Relion)
244,988 extracted segments
Reference-free 2D classification (Relion)
2 cycles
Select particles from good classes (Relion)
3D classification (Relion)
148,876 segments
3D auto-refine
(Relion)
148,876 segments
rise: 42.65 Å
twist: 13.24°
Initial model
(Relion)
Post-processing
(Relion)
Mask
Imposed helical
symmetry (Relion)
4.1 Å
EMD-0298
F
Unmasked map
Corrected map
Fourier Shell Correlation
FSC0.143 = 4.1 Å
Resolution (1/Å)
FSC0.5 = 4.1 Å
G
90°
Inside
Outside
180°
N
C
2.5 Å
3.2 Å
3.9 Å
4.6 Å
5.3 Å
H
C
N
I
P154
Q158
L156
H162
M160
D165
F163
A167
Y170
R174
E172
M108
T110
M112
N113
L115
W118
V117

Fig. S7. Cryo-EM data collection, image processing, and model building for VLP. (**A**) Negative-stain TEM micrograph of VLPs. Inset: a close-up of one VLP segment. (**B**) Cryo-EM micrograph of VLPs. (**C**) Examples of VLP 2D class averages. **(D)** Sum of the power spectra obtained for 26 selected VLP segments. (**E**) Flowchart of the data collection and processing of VLP sample. (**F**) Fourier shell correlation (FSC) curves for the final reconstruction of VLP density map (above) and between VLP reconstructed model and density map (below). (**G**) Local resolution analysis of one ring extracted from VLP filament (above) and one CP unit (below), estimated using MonoRes (*34*). (**H**) Cryo-EM-derived atomic model of the VLP CP fit into extracted map for one CP unit. (**I**) The densities of two VLP CP segments are shown in a mesh representation with the corresponding atomic model within, showing the resolution of individual side chains (maps contoured at 5σ).

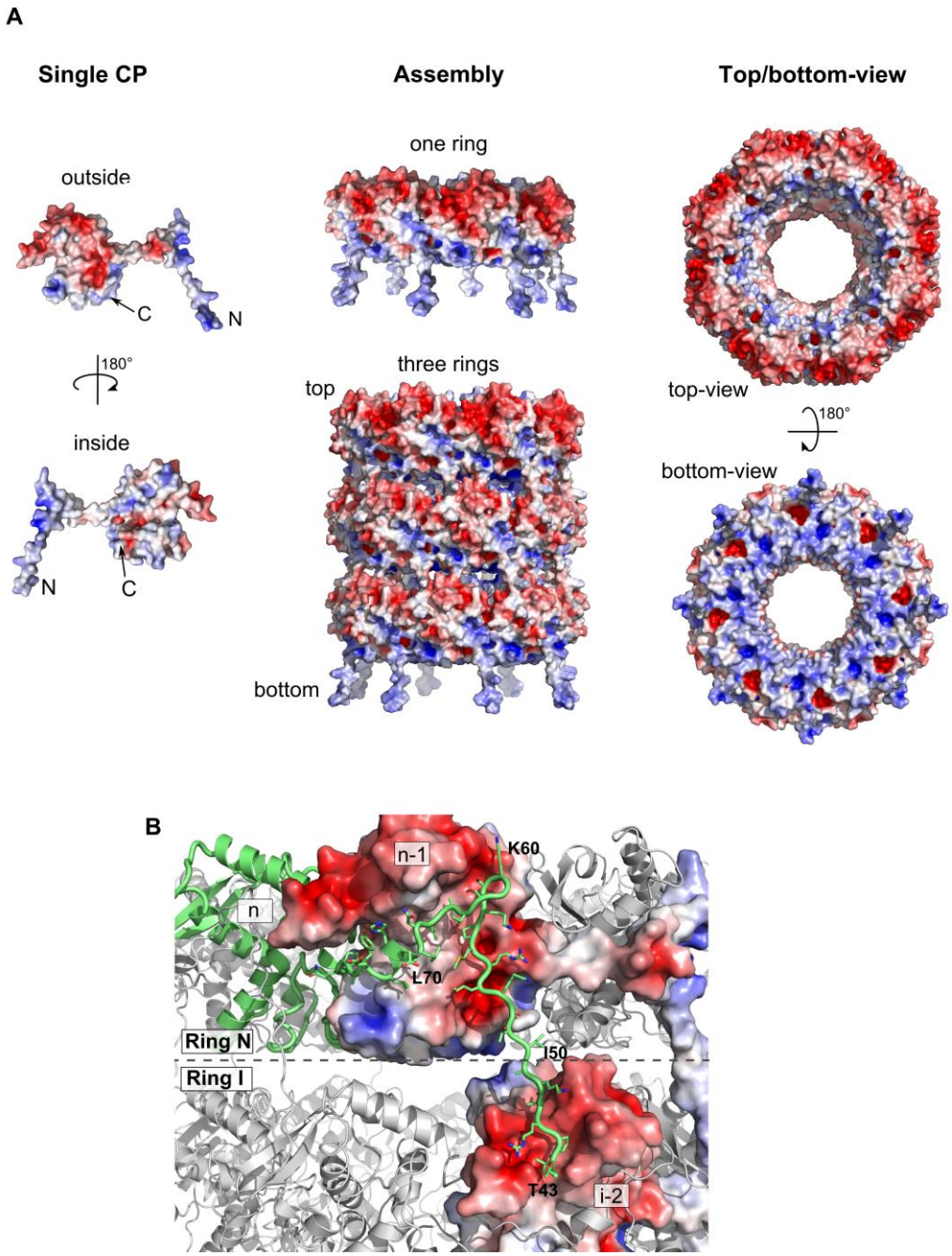

Fig. S8. Surface electrostatic potential of VLPs. (**A**) Surface electrostatic potential of single CP unit, views at two angles (left); CP units assembled into one ring (above center) and rings assembled into the filament (below center). Right: top- and bottom-view of the octameric ring. Red, negative charge; blue, positive charge. (**B**) Assembly of CP^{n} unit (green) with positively charged N-terminal region folding on the negatively charged surfaces of CP^{n-1} and CP^{i-2} cores.

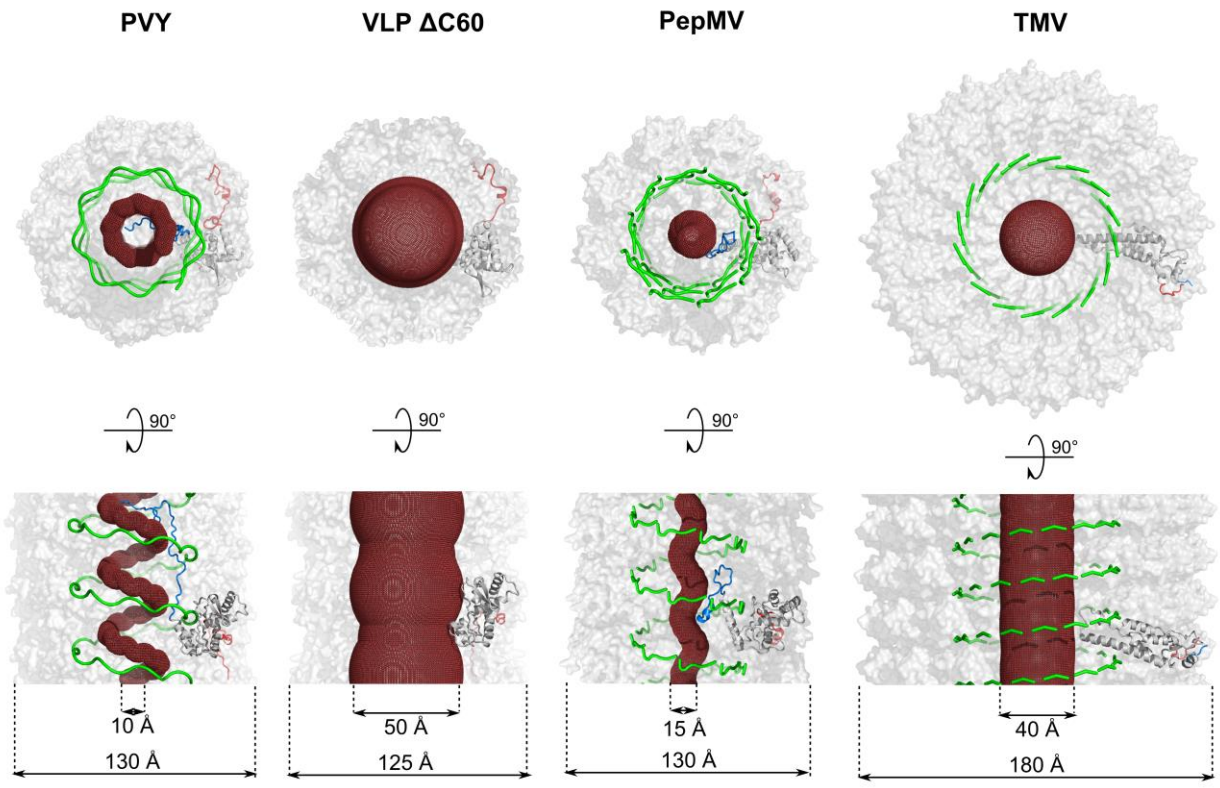

Fig. S9. Water channels in different types of filamentous particles. Differences in size and shape of the channels in potyvirus PVY, potexvirus PepMV, tobamovirus TMV and PVY VLP ΔC60 are presented as side-views and top-views. Channels (dark red dot mesh) are superimposed onto filament silhouette with one copy of CP (N-terminal region in red, core in gray, C-terminal region in blue) and RNA (green), to demonstrate particle assembly. Channels were calculated with MOLE 2.5 (https://mole.upol.cz/).

Table S1. Cryo-EM data collection and refinement statistics of PVY and VLP.

	PVY	VLP
Data collection		
EM equipment	FEI Titan Krios	
Voltage (kV)	300	
Detector	Falcon II	
Pixel size (Å)	1.061	
Electron dose ($e^-/Å^2$)	48	
Defocus range (μm)	1.0-2.2	
Reconstruction		
Software	EMAN2.1, RELION 2.0 & 2.1	
Initial no. of helical segments	215,123	244,988
Final no. of helical segments	162,213	148,876
Initial model used	Geometrical model	Featureless cylinder
Symmetry	C1	C8
Helical symmetry		
Translation (Å)	3.95	42.65
Rotation (°)	-40.95	13.24
Map resolution (Å) at FSC = 0.143	3.4	4.1
Map sharpening B-factor ($Å^2$)	-200	-400
Model building		
Software	Coot 0.8.8	
Refinement		
Software	Phenix 1.13-2998	
Model statistics		
No. of coat protein copies	35	24
No. of residues per coat protein	224 (Val44 – Met267)	176 (Thr43 – Ile218)
No. of RNA nucleotides	175	0
Model resolution (Å) at FSC = 0.5	3.6	4.1
Validation		
Cross-correlation coefficient (CCC)	0.819	0.775
MolProbity score	1.93	1.48
Clashscore	8.18	0.37
R.m.s. deviations		
Bond length (Å)	0.008	0.009
Bond angle (°)	1.389	1.314
Ramachandran plot statistics (%)		
Preferred	91.89	86.73
Allowed	8.11	13.27
Outlier	0	0
Rotamer outliers	0.28	1.95

Table S2. Primers and probes used for in planta functional analysis of PVY mutants and their properties.*

Name	Primer and probe sequences (5' → 3')	Source	Target gene(s)	Description	Amplicon efficiency
PVY_N605	CATAGGAGAAACTGAAATGCCAACT TGGCGAGGTTCCATTTTCA FAM-TGATGAATGGGCTTATGGTTTGGTGCA-TAMRA	this work (*59*) (*59*)	AJ390300	PVY CP	97%
COX	CGTCGCATTCCAGATTATCCA CAACTACGGATATATAAGRRCCRRAACTG FAM-TGCTTACGCTGGATGGAATGCCCT-TAMRA	(*60*)	Sotub04g015050.1.1	cytochrome oxidase	96%

*according to MIQE (*58*) guidelines.

Data S1. Relative concentration of PVY RNA as measured in the leaves of *N. clevelandii* including tables S3 to S5:

Table S3. Relative concentration of PVY RNA as measured in bombarded leaves of *N. clevelandii* 7 dpb (experiment 1).

Table S4. Relative concentration of PVY RNA as measured in upper nonbombarded leaves of *N. clevelandii* 14 dpb (experiment 1).

Table S5. Relative concentration of PVY RNA as measured in bombarded leaves of *N. clevelandii* (experiment 2).